# Journal of Materials Chemistry C

Accepted Manuscript


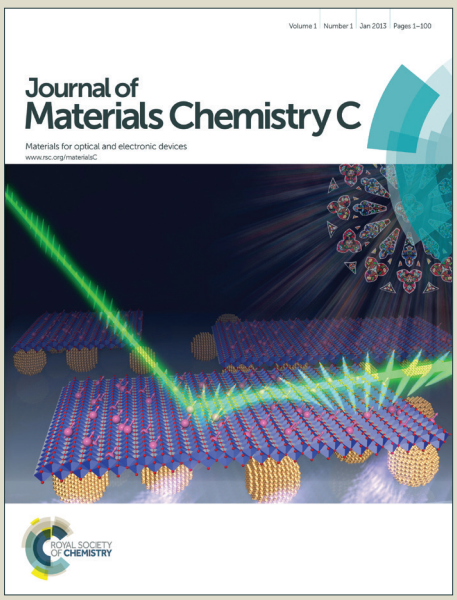





ROYAL SOCIETY OF CHEMISTRY

www.rsc.org/materialsC

# Computational Exploration of Newly Synthesized Zirconium Metal-Organic Frameworks UiO-66, 67, 68 and Analogues

Li-Ming Yang*[†], Eric Ganz,[§] Stian Svelle[‖], and Mats Tilset*[†]

*Dedicated to Professor Henry F. Schaefer, III on the occasion of his 70th birthday*

[†]*Center of Theoretical and Computational Chemistry, Department of Chemistry, University of Oslo, P.O. Box 1033 Blindern, N-0315 Oslo, Norway,* [§]*Department of Physics, University of Minnesota, Minneapolis, Minnesota, USA,* [‖]*in Gap Center of Research Based Innovation, Department of Chemistry, University of Oslo, P.O. Box 1033 Blindern, N-0315, Oslo, Norway.*

(E-mail of corresponding authors: *lmyang.uio@gmail.com* and *mats.tilset@kjemi.uio.no*; Fax: +47 22855441)

**Abstract:** One of the major weakness of metal organic framework (MOF) materials is their rather low thermal, hydrothermal, and chemical stabilities. *Identification of stable and solvent resistant MOF materials will be key to their real world utilization.* Recently, Lillerud and coworkers reported the synthesis of a new class of Zr MOF materials. These materials have very high surface area and exceptional thermal stability, are resistant to water and some solvents, acids, bases, and remain crystalline at high pressure. The newly synthesized Zr metal-organic frameworks (UiO-66, 67, 68) as well as analogues substituting Ti and Hf for Zr, are explored using density functional theory calculations. Crystal structure, phase stability, bulk modulus, electronic structure, formation enthalpies, powder X-ray diffraction, chemical bonding, and optical properties are studied. We find bulk moduli of 36.6, 22.1, 14.8 GPa for UiO-66, -67, and -68 respectively. As the linkers are extended, the bulk modulus drops. The highest occupied crystal orbital to lowest unoccupied crystal orbital gaps range from 2.9 to 4.1 eV. The compounds have similar electronic structure properties. Experimental powder x-ray diffraction patterns compare well with simulation. The large formation enthalpies (–40 to –90 kJ/mol) for the series indicate high stability. This is consistent with the fact that these materials have very high decomposition temperatures. A detailed analysis of chemical bonding is carried out. Potential applications for these new materials include organic semiconducting devices such as field-effect transistors, solar cells, and organic light-emitting devices. We hope that the present study will stimulate research in UiO-based photocatalysis and will open new perspectives for the development of photocatalysts for water splitting and $CO_2$ reduction. The large surface areas also make these materials good candidates for gas adsorption, storage, and separation.

## I. Introduction

Metal organic frameworks (MOFs),[1,2] composed of metal ions or metal clusters as nodes and organic linkers have received considerable attention and achieved explosive development due to their wide applications in gas adsorption, storage, separation, catalysis, sensing, molecular recognition, drug delivery, and biomedicine.[1,2] Although the structure and internal environment of pores can be in principle controlled through judicious selection of nodes and organic linkers, and the direct synthesis of such materials with desired functionalities in the pores or channels is often difficult to achieve due to their thermal/chemical sensitivity or high reactivity. New MOFs appear at a very high pace[3] using novel preparation techniques. Tens of thousands MOFs have already been reported, but the appearance of new, stable inorganic building bricks is rare. Up to now, only few highly symmetric inorganic building units have been reported, i.e., $Cu_2(OH)_2(CO_2)_4$ in HKUST-1,[4] $Zn_4O(CO_2)_6$ in MOF-5 (aka IRMOF-1)[5] *via* the elegant isoreticular synthesis of the IRMOF series,[6] and $Cr_3O(OH)_3(CO_2)_6$ from MIL-88.[7]

It is known to the chemical community that the major weakness of the MOF materials is their rather low thermal, hydrothermal, and chemical stabilities when compared with zeolites. This fact is undoubtedly limiting their use in large scale industrial applications. *Identification of stable and solvent resistant MOF materials will be key to their real world utilization.*

Recently, Lillerud *et al.*[8] reported the synthesis of a new class of Zr MOF materials. They introduced a new inorganic building brick $Zr_6O_4(OH)_4(CO_2)_{12}$ which forms metal organic frameworks UiO-66, 67, 68. These materials have very high surface area and exceptional thermal stability, are resistant to water and some solvents, and remain crystalline at high pressure.[9] Subsequently, Silva, et al.[10] described the photocatalytic hydrogen generation of water/methanol using UiO-66 and UiO-66-$NH_2$ as photocatalysts. Wang, et al.[11] studied the adsorption of $CH_4$ and $CO_2$ on UiO-66. Gross's and Serre's groups[12] reported the low-temperature synthesis of porous zirconium (IV) dicarboxylates by the exchange of the monocarboxylate ligand of the zirconium methacrylate oxocluster $Zr_6O_4(OH)_4(OMc)_{12}$ (OMc = $CH_2$=$CH(CH_3)COO$) with dicarboxylic acids. Groppo, et al.[13] described the formation and stability of (arene) $Cr(CO)_3$ species inside UiO-66. Maurin, et al.[14] computationally studied the ligand functionalization effect on the $CO_2/CH_4$ separation performance of UiO-66. Jobic's and Maurin's groups[15] probed the dynamics of $CO_2$ and $CH_4$ within UiO-66 using a combination of neutron scattering measurements and molecular simulations. Llewellyn's and Maurin's groups[16] explored the thermodynamic and kinetic behavior of $CO_2/CH_4$ gas mixture

within UiO-66.

Lillerud's and Lamberti's groups[9] made a detailed characterization of the UiO-66 material *via* powder x-ray diffraction (PXRD), Extended X-Ray Absorption Fine Structure (EXAFS), infrared, ultraviolet-vis spectroscopies and density functional theory (DFT) calculations. Bárcia, et al.[17] studied the reverse shape selectivity in the adsorption of hexane and xylene isomers in UiO-66. Behrens et al.[18] explored the influence of benzoic acid, acetic acid, and water on the synthesis of Zr-MOFs. Tilset, et al.[19] discussed the post-synthetic modification of UiO-66. Amino (-$NH_2$), bromo (-Br), and nitro (-$NO_2$) functionalized UiO-66 have been reported in the Lillerud's group,[20] which still retain high thermal and chemical stabilities. Amino (-$NH_2$), bromo (-Br), nitro (-$NO_2$), and naphthalene (-1,4-Naph) functionalized UiO-66 have been reported in Cohen's group.[21] Hydrogen storage in UiO-66 and -67 has also been reported in Lamberti's group.[22] The interpenetrated Zr-MOFs have been synthesized and characterized by Godt, Behrens, and coworkers.[23] Gianolio et al.[24] described high resolution EXAFS results on UiO-66, 67, 68.

Hafnium-based materials including Hf-UiO-66 have also been fabricated by Jakobsen et al.[25]. They also carried out high resolution X-ray studies of the structure of the material. Furthermore, sulfone-functionalized Zr/Hf-UiO-67 have been fabricated by Trikalitis et al.[26] for $CO_2$ adsorption. Finally, Wu et al.[27] have studied the shear strength of the UiO-66, 67, 68 materials including Zr, Ti, and Hf and concluded that these materials have remarkably high shear strength.

Vermoortele et al.[28] used synthesis modulation to increase the catalytic activity of UiO-66. Ragon et al.[29] have fabricated 0.5 kg quantities of UiO-66. Falkowski et al.[30] created a UiO-66 variant using a BINAP-derived dicarboxylate linker. This was synthesized and post-synthetically metalated with Ru and Rh complexes to afford highly enantioselective catalysts for important organic transformations. Feng et al.[31] created a new series of materials PCN-224 by substituting metalloporphyrins for the linkers in UiO-66. Remarkably, PCN-224(Co) exhibits high catalytic activity for the CO2/propylene oxide coupling reaction and can be used as a recoverable heterogeneous catalyst. He et al.[32] investigated using UiO MOFs as potential nanocarriers for anticancer drugs.

In the present work, we performed a comprehensive computational study on the crystal structure, phase stability, electronic structure, chemical bonding, formation enthalpies, mechanical, and optical properties of the M-UiO-66, 67, 68 (M = Ti, Zr, and Hf) series using DFT calculations in the Vienna *ab initio* simulation package (VASP) code.[33-36] The optical properties were calculated using the CASTEP module[37] of the Material Studio 5.0 program.[38]

This study will provide valuable insights into these novel UiO materials for potential use in gas separation and storage, photocatalysis, photoactive materials for photovoltaic cells, and as components for electroluminescence or other optical devices.

## II. Computational methodology and details

The VASP[33-36] code was used for the total-energy calculations to study the structural stability and to establish equilibrium structural parameters. The generalized gradient approximation (GGA)[39-41] includes the effects of local gradients in the charge density for each point in the material and generally gives better equilibrium structural parameters than the local density approximation (LDA). Hence, the Perdew, Burke, and Ernzerhof (PBE)[41] GGA functional was used for all calculations. The projector-augmented-wave (PAW)[42,43] pseudo-potentials were used to describe the ion-electron interactions. A criterion of 0.01 meV $atom^{-1}$ was placed on the self-consistent convergence of the total energy and all calculations were made with plane-wave cutoff of 500 eV, which guarantees that absolute energies are converged to within a few meV/f.u. This has been tested to be accurate and reliable for our M-UiO-66, 67, 68 (M = Ti, Zr, and Hf) series systems. Brillouin-zone integration was performed with a Gaussian broadening of 0.2 eV during all relaxations. The highly efficient conjugate-gradient algorithm based on Hellmann-Feynman forces was used to relax the ions into their instantaneous equilibrium positions. The forces and the stress tensor were used to determine the search directions for finding the equilibrium positions (the total energy was not taken into account). Forces on the ions were calculated using the Hellmann–Feynman theorem as the partial derivatives of the free electronic energy with respect to the atomic positions and adjusted using the Harris–Foulkes correction to the forces. The atoms were relaxed toward equilibrium until the Hellmann-Feynman forces were less than $10^{-3}$ eV $Å^{-1}$.

The Ti and Hf models were created by direct atomic substitution of the elements for the Zr atoms in the Zr models. Calculations were performed on the primitive cells. Because we are dealing with a large system, the **Γ**-point alone was sufficient for sampling the Brillouin zone during geometry optimization. DOS calculations were performed with **Γ**-point *via* using Monkhorst–Pack scheme and 'high precision'. We set the parameter NEDOS for DOS calculations to a high value (801). For the hafnium calculations, the *f*-electrons were in the frozen core, using the standard VASP PAW pseudo-potential.

Bond overlap population (BOP) values were calculated with on the fly pseudopotential as implemented in CASTEP.[37] Charge density, charge transfer, and electron localization function (ELF)[44-47] analyses were also performed. We have also calculated the linear optical properties

including dielectric function, absorption coefficient, reflectivity, refractive index, optical conductivity, and energy loss function, and band structure with ultrasoft pseudopotential in CASTEP. These methods have been previously used in our group.[48-57]

## III. Results and discussion

### A. Crystal Structure Details

The crystal structures of the experimentally realized UiO-66, 67, 68 materials were initially solved from powder X-ray diffraction data (PXRD). In the 2008 experimental work on Zr-UiO-66, it was found that after the removal of guest atoms, one is left with a hydroxylated system. (After heating in vacuum one can achieve a dehydroxylated system, which we will not discuss.) In the actual (experimental) hydroxylated system, the PXRD cannot locate the positions of hydrogen atoms due to the low electron density of H atoms. Thus, the symmetry of the space group for UiO-66, -67, -68 was assigned to *Fm-3m* based on the experimental PXRD pattern.[9] Hydrogen atoms cannot be located in the PXRD structure refinement, but charge balancing requires the presence of four OH groups, and the presence of OH groups is also evident from the IR data (the characteristic adsorption of OH was seen at 3675 $cm^{-1}$).[8] The symmetry of the computational model will be determined by how these four $\mu_3$−OH groups, and four $\mu_3$−O groups are added to the system.

In the actual (experimental) hydroxylated system, the Zr clusters do not show preferential ordering, resulting in the same observed symmetry space group for the UiO-66, UiO-67, and UiO-68 frameworks (*Fm-3m*). For the periodic DFT calculations, one must choose how to orient the four $\mu_3$−OH groups, and the four $\mu_3$−O groups, as already discussed by Valenzano et al.[9] Thus, the space symmetry groups employed in the calculations on the hydroxylated system reported here are *F-43m*, *P-43m*, and *F-43m* for UiO-66, UiO-67, and UiO-68, respectively. We note that Chavan et al.[22] modeled UiO-67 in the *F23* space group as opposed to the *P-43m* space group employed here.

Another consideration is that in the experimental case, the sample is at room temperature and therefore the phenyl rings can rotate. Each configuration corresponds to a specific point in the potential energy surface with specific energy. However, our calculations were performed based on a single stable configuration of a perfect hydroxylated crystal at 0K.

The exceptional thermal stability ($T_{decomp}$ = 540 °C)[8] of Zr-MOF is mainly ascribed to the inorganic brick. This element is 12-fold coordinated, the highest coordination reported for a MOF. This new brick consists of an inner $Zr_6(\mu_3{-}O)_4(\mu_3{-}OH)_4$ core in which the triangular

faces of the $Zr_6$-octahedron are alternatively capped by $\mu_3$−O and $\mu_3$−OH groups. This stability is also reflected in the high bulk modulus that we calculate, as well as the unusually large shear modulus discussed by Wu et al.[27]

The Zr-MOFs series shows scale chemistry. By increasing the length of the linkers, we can make UiO-67 (ligand is 4,4'-biphenyl-dicarboxylate (BPDC)) and UiO-68 (ligand is terphenyl dicarboxylate (TPDC)). Remarkably, the materials with larger pores are still thermally stable. These materials demonstrate the ultimate thermal stability currently obtainable for hybrid frameworks with organic linkers.

The Langmuir surface area of UiO-66 is 1187 $m^2/g$.[8] Increasing the length of the linkers is a route to create high surface area materials, the surface area of the material increases to 3000 for UiO-67 and 4170 $m^2/g$ for UiO-68.[8] The large surface areas make Zr-MOF good candidates for gas adsorption, storage, and separation. The resistance to water and other solvents and the general toughness of these lattices is an important advantage compared to other MOF materials for real world applications. The crystal structures of M-UiO-66, 67, 68 are illustrated in Figure 1.

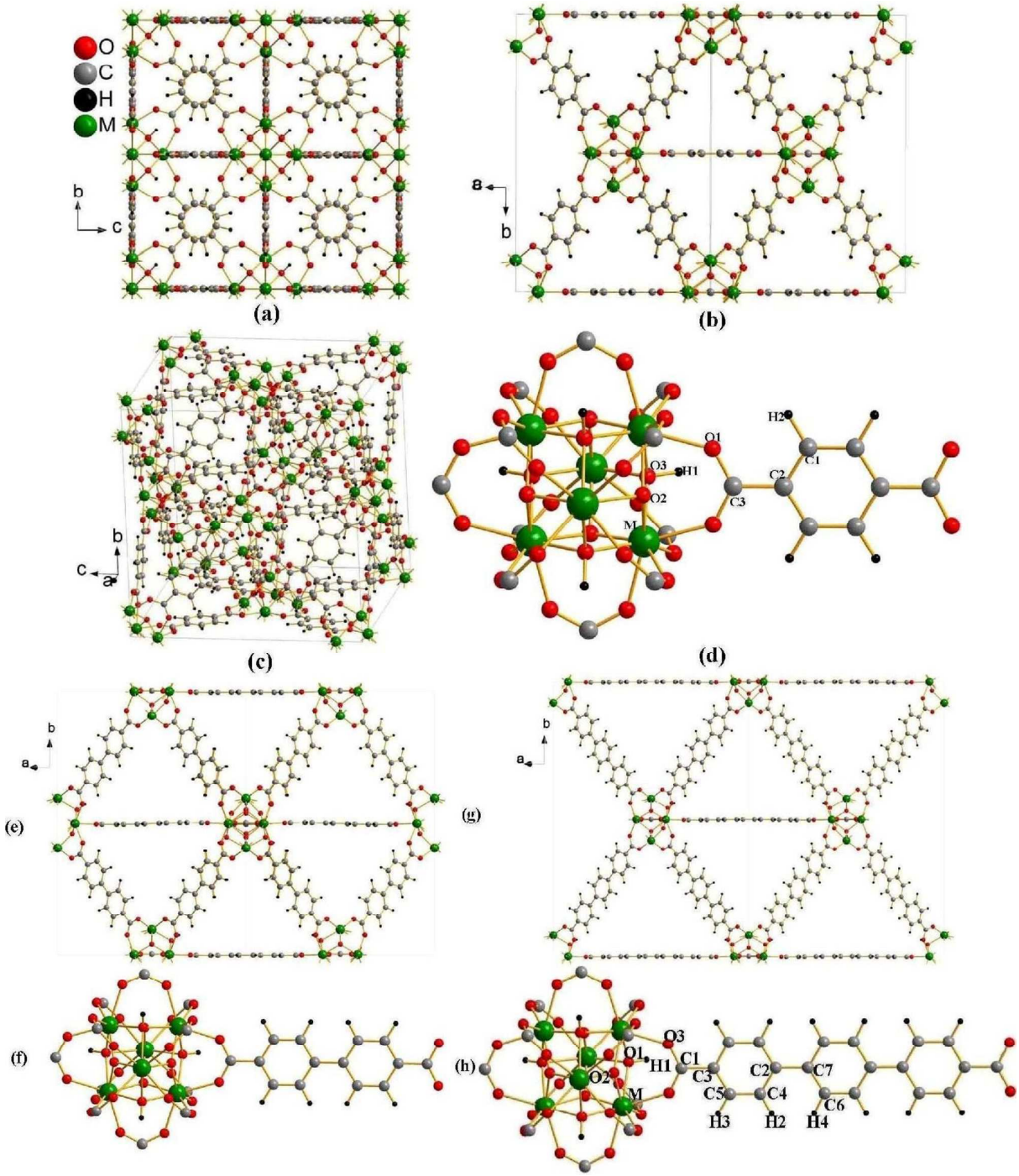


**Figure 1**. The calculated crystal structures of UiO-66 in (a) to (d), UiO-67 in (e) and (f), and UiO-68 in (g) and (h). We distinguish the atoms with labels M, O1, O2, O3, C1, C2, C3, H1, and H2 for M-UiO-66. For M-UiO-68, the atomic labels are M, O1, O2, O3, O4, C1, C2, C3, C4, H1, H2, and H3. The crystal structure of UiO-67 is more complicated than that of UiO-66 and -68 due to lower symmetry.

### B. Crystal Structure Optimization

We started with the experimental structures of Zr-UiO-66, 67, 68 determined from PXRD and then fully hydroxylated the structure using Material Studio.[38] These structure were fully

optimized using the appropriate symmetry. Then, to extend to the other models we replaced the Zr atoms with tetravalent metal atoms Ti and Hf. These were again optimized to achieve ground-state structures of M-UiO-66, 67, 68 (M = Ti and Hf).

This was achieved by first relaxing the atomic positions globally using the force-minimization technique, i.e., by keeping the lattice constant ($a$) and cell volume (V) fixed to experimental values. Then the theoretical ground-state volume was determined from total energy minimization by varying the cell volume within ±10% of the experimentally determined volume where the atom positions were relaxed for each volume step. The calculated total energy as a function of volume was fitted to the Birch–Murnaghan equation of state (BMEOS)[58] to calculate the bulk modulus ($B_0$) and its pressure derivative ($B_0'$). We see that the bulk modulus decreases from 36.6 GPa to 22.1 GPa to 14.8 GPa as we go from UiO-66 to UiO-67 and -68. These values agree well with the computational results of Wu et al.[27] The pressure derivative stays relatively constant between 4.3 and 4.6.

For MOF-5 (with BDC linkers), the bulk modulus is 15.4 GPa with B' = 5.1.[48] The bulk moduli of the UiO-66 and -67 series are much larger than that of MOF-5. Whereas, the bulk modulus of the M-UiO-68 series (with longer linkers) is comparable to that of MOF-5. We can also compare to the bulk modulus of IRMOF-10 which is 9.1 GPa.[50] The bulk modulus of M-UiO-67 is much larger than that of IRMOF-10 which has the same linker. We can see (**Fig. S1**) that the bulk modulus of the UiO series is larger than the IRMOF materials due to the different topology which has 12-fold coordinated corners.

For M-UiO-66, the conventional cell with chemical formula $(M_6O_{32}C_{48}H_{28})_4$ contains 456 atoms, and is a face centered cubic cell with space group *F-43m*. For M = Zr, the lattice parameter of conventional cell is $a$ = 20.7194 Å, which is quite close to the experimental result $a$ = 20.7004 Å. For M-UiO-68, the chemical formula is $(M_6O_{32}C_{120}H_{76})_4$, $a$ = 32.7969 Å, the conventional cell has 936 atoms, *F-43m.* For M = Zr, our calculated lattice parameter is $a$ = 33.3063 Å. For M-UiO-67, with a lattice parameter $a$ = 26.8644 Å (experimental data), the space group is *P-43m*. The chemical formula for the conventional cell of UiO-67 is $Zr_{24}O_{128}C_{336}H_{208}$, which is a simple cubic unit cell, the conventional cell is already a primitive cell. The total number of atoms is 696. All the calculated results are based on the hydroxylated form of a perfect crystal desolvated from the experimentally as-synthesized sample. Here, we do not consider partial occupancy or defects in the sample, which is beyond the scope of current study.

**Table 1.** Optimized equilibrium lattice constant ($a$ (Å)), bulk modulus ($B_0$ (GPa)), and its

pressure derivative ($B_0$') for M-UiO-66, 67, 68 (M = Ti, Zr, and Hf).

| Materials | $N_c$ | $N_p$ | SG | CS | $a$ (Å)[a] | $B_0$ (GPa)[b] | $B_0$' |
|---|---|---|---|---|---|---|---|
| (Ti, 66) | 456 | 114 | *F-43m (216)* | FCC | 20.38 | 38.28 <42.07>[27] | 5.11 |
| (Zr, 66) | 456 | 114 | *F-43m (216)* | FCC | 20.96 <20.70>[8] | 36.62 <41.01>[27] | 4.33 |
| (Hf, 66) | 456 | 114 | *F-43m (216)* | FCC | 20.83 <20.70>[25] | 37.55 <39.49>[27] | 4.94 |
| (Ti, 67) | 696 | 696 | *P-43m (215)* | SC | 26.57 | 22.79 | 4.22 |
| (Zr, 67) | 696 | 696 | *P-43m (215)* | SC | 27.14 <26.86>[8] | 22.10 <17.15>[27] | 4.70 |
| (Hf, 67) | 696 | 696 | *P-43m (215)* | SC | 27.02 | 22.61 | 5.08 |
| (Ti, 68) | 936 | 234 | *F-43m (216)* | FCC | 32.73 | 15.25 | 5.05 |
| (Zr, 68) | 936 | 234 | *F-43m (216)* | *FCC* | 33.31 <32. 80>[8] | 14.80 <14.40>[27] | 4.58 |
| (Hf, 68) | 936 | 234 | *F-43m (216)* | FCC | 33.17 | 15.10 | 5.77 |

[a] $N_c$ is the number of atoms per conventional cell, $N_p$ is the number of atoms per primitive cell, SG is the space group, CS is the crystal system. FCC is face-centered cubic, SC is simple cubic. Data in <> are experimental lattice parameters.
[b] Data from Birch-Murnaghan 3rd-order EOS. Data in <> are computational results from Wu et al.[27]

Titanium, Zirconium and Hafnium belong to the same group in the periodic table. The main difference between Hf and Zr in terms of electronic structure is the *f* states. Hf has a closed 4*f* subshell, whereas Zr has no *f* electrons. Because of the "lanthanide contraction", Zr and Hf are often regarded as the two chemically most similar homogenesis elements.[59] We know the atomic radius of Zr and Hf are 160 pm and 159 pm, respectively, which are much larger than that of Ti (147 pm). For this reason we predicted that Hf should substitute readily for Zr in the UiO-66 series. In fact, this is true and the Hf-UiO-66 material has recently been fabricated.[25] Also, a mixed Hf and Zr-UiO-66 material has been fabricated.[60] We have discussed above some of the interesting properties of Ti-based MOFs and oxides. Therefore if it is possible to create Ti-UiO materials, then they may have very desirable and interesting optical or photocatalytic properties. For example, Ti is lightweight and inexpensive.

The optimized atomic positions, calculated equilibrium lattice parameter with the corresponding experimental values are listed in **Table 1**. From Ti to Hf to Zr, the optimized equilibrium lattice constant increases, which is consistent with the increasing atomic radii of the central metal atoms. We can see that the calculated lattice constants agree well with available experimental data.

The optimized atomic positions (xyz coordinates) and calculated equilibrium lattice parameters along with the corresponding experimental values are listed in **Table S1**. From **Table S1**, we can see the results are comparable between the experimental data and our calculations. Encouragingly, Lillerud's and Lamberti's groups[9] made a detailed characterization of UiO-66 *via* XRPD, EXAFS, IR, UV-vis spectroscopies and DFT-B3LYP calculations (with CRYSTAL code). We can also compare the B3LYP-CRYSTAL results

with our PBE-GGA-VASP data, which will give us confidence to make reliable prediction for the analogues. The detailed information was listed in **Table S1**, from which we can see the computational results are almost identical.

The comprehensive results of the VASP optimized geometry parameters at equilibrium volumes as well as experimental ones can be found in **Table S2**, using the atomic labels shown in **Scheme S1**. From **Table S2**, we can see that the calculated geometric parameters are generally comparable to the experimental data.

### C. X-ray Diffraction Results

The agreement between the VASP optimized structures and experimental data can also be tested by comparing predicted powder X-ray diffraction patterns for the calculated structures with those of the experimentally determined ones. We simulated the PXRD patterns for the whole series. **Fig**. **S2(a)**, **S2(c)**, and **S2(e)** display the experimental PXRD pattern based on the experimental synthesized samples for the Zr-UiO-66, Zr-UiO-67, Hf-UiO-66 materials, respectively. **Fig**. **S2(b)**, **S2(d)**, and **S2(f)** display the computationally simulated PXRD pattern based on the optimized solid-state crystal structures for these materials. In general, the experimental and simulated PXRD patterns agree well with each other (**Fig. 2S**). In particular, the peak positions and relative heights are in good agreement for the Zr materials. If we compare the PXRD patterns from Zr-UiO-66, Zr-UiO-67, and Zr-UiO-68 (shown in SI), then we see that as we go to the larger linkers, the higher angle PXRD peaks move to smaller angles. Finally, for the Hf-UiO-66 material, we see good agreement in the peak positions, but substantial difference in the relative peak heights. For the remaining materials, the results are in **Fig. S2(g)-(l).**

**Formation Enthalpy and Synthesis Considerations**

Zr-UiO-66, 67, 68[8] and Hf-UiO-66[25] have been experimentally synthesized, and are therefore known to be stable materials. In our previous work, we found that data on formation enthalpies constitute an excellent means to establish whether theoretically predicted phases are likely to be stable and such data may serve as a guide to evaluate possible synthesis routes.[48-52] For the exploration of the thermodynamic feasibility of accessing these compounds from the constituents (eqs. 1, 2, and 3) we have computed the total energies for C, $O_2$, $H_2$, Ti, Zr and Hf in their ground state structures. The reaction enthalpies for MOFs formation were calculated from the difference in the total energy between the products and reactants. The

results unambiguously establish that equations 1, 2, and 3 expresses exothermic reactions for all materials.

$6M + 16O_2 + 48C + 14H_2 \rightarrow M_6O_{32}C_{48}H_{28}$, (M-UiO-66, M = Ti, Zr, Hf) (1)

$24M + 64O_2 + 336C + 104H_2 \rightarrow M_{24}O_{128}C_{336}H_{208}$, (M-UiO-67, M = Ti, Zr, Hf) (2)

$6M + 16O_2 + 120C + 38H_2 \rightarrow M_6O_{32}C_{120}H_{76}$, (M-UiO-68, M = Ti, Zr, Hf) (3)

**Table 2.** Calculated enthalpies of formation ($\Delta H$; kJ $mol^{-1}$) per formula unit according to equations 1, 2, 3 for the M-UiO-66, 67, 68 (M = Ti, Zr, and Hf) compounds

| M | Ti-66 | Zr-66 | Hf-66 | Ti-67 | Zr-67 | Hf-67 | Ti-68 | Zr-68 | Hf-68 |
|---|---|---|---|---|---|---|---|---|---|
| $\Delta H$ (kJ $mol^{-1}$) | -76.9 | -86.9 | -89.4 | -50.7 | -57.2 | -58.9 | -37.6 | -42.5 | -43.7 |

The formation energy can be effectively tuned *via* different combination of nodes (from Ti to Zr to Hf) and linkers (from BDC to BPDC to TPDC). The formation energy (**Fig. 2**) increases when moving from UiO-66, -67, -68 and from Ti to Hf. From **Table 2** we can see that these formation energies are large and negative, demonstrating the high stability of the UiO series. It is notable that the recently synthesized Zr-UiO-66, -67, -68 materials demonstrate remarkable stability at high temperatures, high pressures and in presence of different solvents acids and bases.[9] Furthermore, a highly stable Hf-UiO-66 was synthesized with possible application to interim radioactive waste scavenging.[25] The fact that so many of these materials have already been fabricated suggests that the remaining materials (including Ti) show good promise for fabrication.

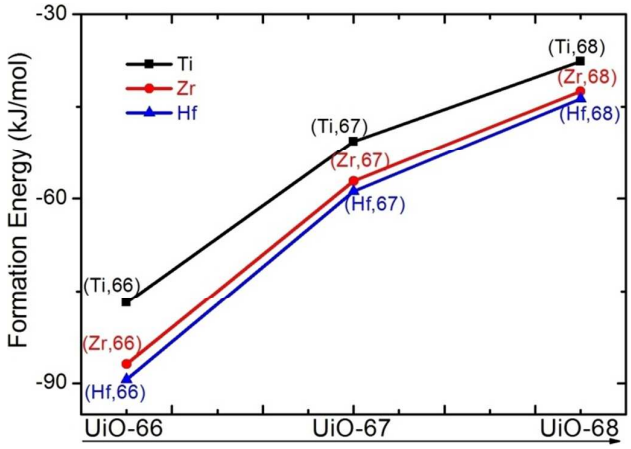


**Figure 2**. Formation energy of M-UiO-66, -67, -68, (M=Ti, Zr, Hf)

Considering the titanium materials specifically, a series of novel MOFs with titanium -based nodes, although with different topologies have been synthesized.[61-65] It should be pointed out that as a constituent of MOFs, the nodes mainly correspond to divalent and trivalent ions of 3*d* transition metals, among them, titanium is a very attractive candidate due to its low toxicity, redox activity, and photocatalytic properties. A typical example is titanium 1,4-benzenedicarboxylate (or terephthalate) MIL-125(Ti)[61] which has several interesting properties, i.e., high thermal stability (633 K), its porous character ($S_{BET}$ = 1550 $m^2/g$), its composition, and its photocatalytic properties, making it an attractive candidate for numerous applications. Additionally, post-synthetic modification materials, such as $NH_2$-MIL-125(Ti),[62] have shown very interesting properties as photocatalysts with visible-light-induced activity for $CO_2$ reduction, and have promising applications for the reduction of $CO_2$. Additionally, Baranwal, et al.[63] reported the shape controlled synthesis of nano-sized titanium (IV) MOFs. Moreover, Rozes, et al.[64] demonstrated that $Ti_8O_8(OOCR)_{16}$ is a new family of titanium-oxo clusters: providing a new natural building unit for reticular chemistry. Frey, et al.[65] prepared new organic-inorganic hybrid fibers (polyvinyl alcohol (PVA)/$HfO_2$) by an electrospinning method using DI water as a solvent.

The combination of the recent interesting experimental progress on photocatalysts using Zr-UiO-66 for water splitting together with the fact that $TiO_2$ is the most widely used photocatalytic material suggests that the experimental synthesis of Ti-UiO-66 MOFs will very likely lead to interesting photocatalytic materials. Ti is also a much lighter element (important for gas storage applications) and also lower cost.

### D. Electronic Structure and band gap engineering

In order to understand the electronic structure and bonding behavior in the entire series, the electronic total density of states (TDOS) and partial density of states (PDOS) of M-UiO-66, 67, 68 are comprehensively studied. The TDOS and PDOS of the Zr-UiO-66 are displayed in **Fig. 3**. The TDOS for the whole series are displayed in **Fig. 4**. The PDOS for Zr-UiO-67, 68, M = Ti/Hf of the M-UiO-66, 67, 68 series can be found in the supporting information (**SI**). These density of states plots have been corrected using the scissors operation described below.

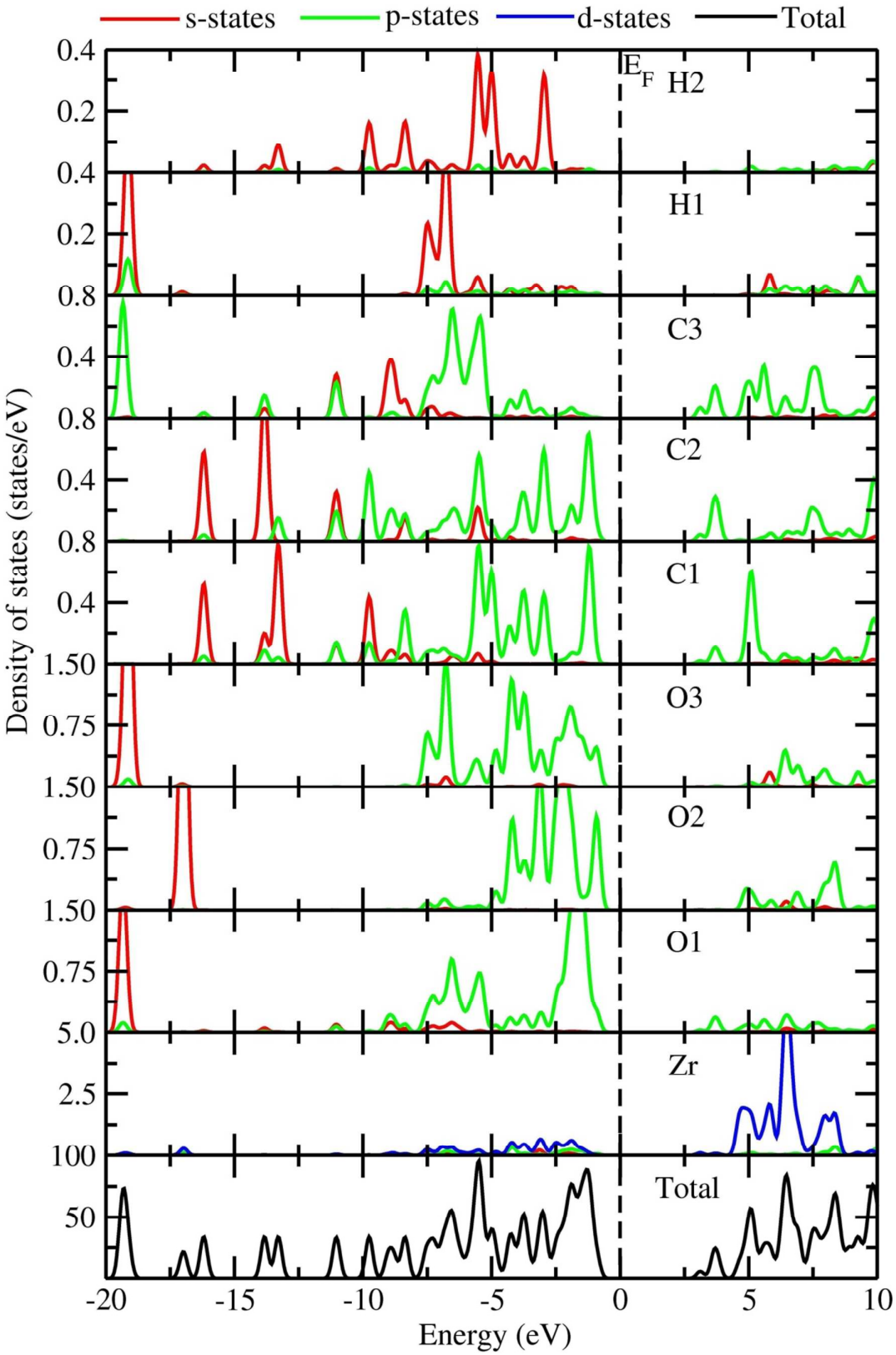


**Figure 3.** The corrected calculated total density of states and partial density of states for Zr-UiO-66.

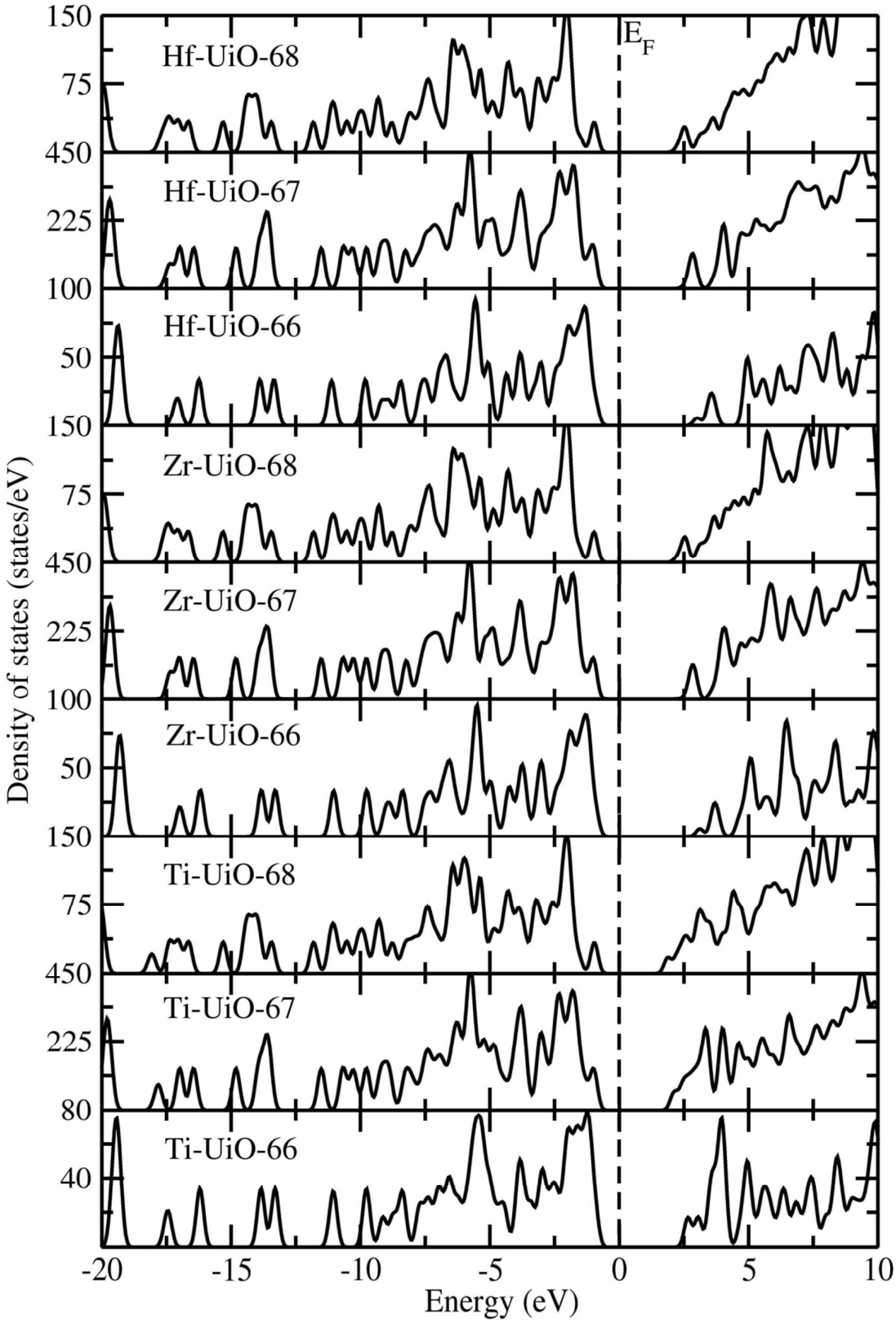


**Figure 4.** Corrected calculated total density of states for M-UiO-66, 67, 68 (M = Ti, Zr, and Hf) series.

**Table 3.** Experimental and predicted HOCO - LUCO gap values for the UiO series. In the final column, we show the predicted gap after applying the scissors operation to the original DFT result.

| Materials | Exp. $E_g$ (eV) | DFT Uncorrected $E_g$ (eV) | *Predicted* $E_g$ (eV) |
|---|---|---|---|
| Ti-UiO-66 | *[a] | 2.63 | 3.64 |
| Ti-UiO-67 | * | 2.44 | 3.23 |
| Ti-UiO-68 | * | 2.11 | 2.92 |
| Zr-UiO-66 | 4.07[9] | 2.94 | 4.07 |
| Zr-UiO-67 | 3.68[22] | 2.78 | 3.68 |
| Zr-UiO-68 | * | 2.34 | 3.23 |
| Hf-UiO-66 | * | 2.70 | 3.74 |
| Hf-UiO-67 | * | 2.69 | 3.57 |
| Hf-UiO-68 | * | 2.31 | 3.19 |

[a]*Indicates no experimental data are available.

The experimental and predicted highest occupied crystal orbital (HOCO) - lowest unoccupied crystal orbital (LUCO) gap values as well as scissor corrected ones are listed in **Table 3**. The uncorrected calculated HOCO - LUCO gap value, $E_g$, for Zr-UiO-66 is 2.94 eV, which is a significantly smaller than the experimental results of 4.07 eV.[9] It should be noted that the band gap values calculated based on density functional theory (DFT) tend to be significantly lower than experimentally determined band gap values.[66] if one has available experimental data, it is possible to correct for this using a scissor operator.[67] The scissor operator $\Delta$ effectively eliminates the difference between the theoretical and experimental gap values by means of a simple rigid shift of the unoccupied conduction band with respect to the valence band. Since the hydroxylated experimental bandgap for Zr-UiO-66 is 4.07 eV,[9] and the uncorrected calculated DFT HOCO - LUCO gap is 2.94 eV, we will use a scissors operator of $\Delta_{Zr\text{-}66}$ = 1.13 eV for the optical properties calculations for Zr-UiO-66. For UiO-66 Ti and Hf, and for UiO-68 Zr, Ti, and Hf the scissors operator is scaled to be $\Delta_{66,\ 68}$ = (uncorrected DFT $E_g$) × 1.13 eV / 2.94 eV. For Zr-UiO-67, the experimental bandgap is 3.68 eV, so the scissors operator for UiO-67 Zr, Ti, and Hf is $\Delta_{67}$ = (uncorrected DFT $E_g$) × 0.90 eV / 2.78 eV. These corrected values will be used in the discussion below.

From **Table 3**, we can see the corrected band gap decreases from 4.1 to 3.7 to 3.2 eV for UiO-66 to -67 to -68. The corrected HOCO - LUCO gaps for the entire series are shown in **Fig. 5**. It is interesting to note that the gap $E_g$ is effectively tuned using different types of metal atoms (M=Ti, Zr, Hf) or linkers (BDC, BPDC, TPDC for UiO-66, -67, -68, respectively). For example, the gap is monotonically decreasing as the material changes from M-UiO-66 to -67 to -68.

For electronic structure calculations in general, some well-known but rough trends in the

determination of the bandgap of elemental semiconductors can be made: HF (Hartree-Fock) generally overestimates gaps[68] while LDA and GGA (e.g., PBE) pure DFT functionals give lower values (roughly by 1 eV) than the experiments.[69-71] This is similar to our result for Zr-UiO-66 (uncorrected DFT $E_g$ = 2.94 *vs*. experimental $E_g$ = 4.07 eV[9]) in the present work. Therefore, if possible, it is very desirable to have experimental comparison when calculating band gaps of novel semiconducting materials. On the other hand, for MOF-5, with flat bands typical of a molecular crystal, we demonstrated,[48] that the uncorrected DFT calculated band gap for MOF-5 agrees quite well with the experimental data.[72]

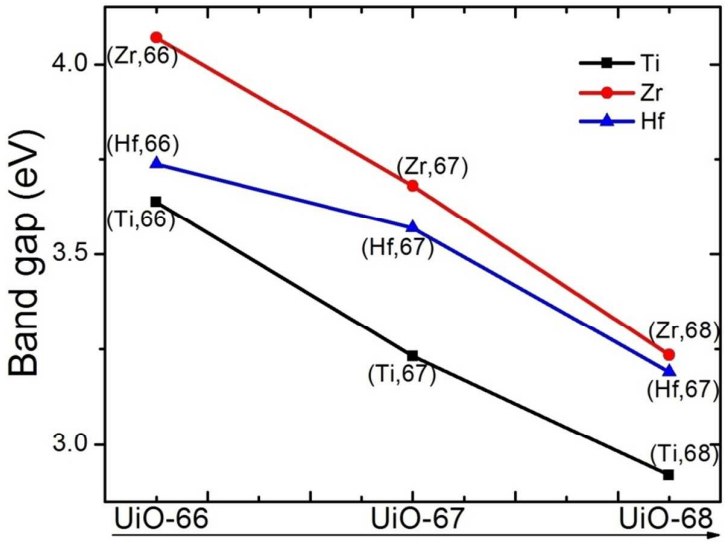


**Figure 5**. Evolution of the calculated corrected band gap of M-UiO-66, -67, -68, (M=Ti, Zr, Hf) series in the equilibrium cubic structure.

The corrected HOCO - LUCO gaps range from 2.9 to 4.1 eV. This indicates that the gap can be tuned by varying the organic linkers. We see that we can effectively tune the band gap over a 1.2 eV range by repeating the benzene units and so extending the linkers. This will in turn tune the optical properties of these materials. These UiO materials may have practical applications as photocatalysts (e.g. for water splitting process). Furthermore, it can be seen that the characteristic peaks of TDOS for all these compounds are very similar which implies that the calculated HOCO - LUCO gaps within the M-UiO-66 to 68 (M = Ti, Zr, and Hf) series have a common structural origin that is similar to M-IRMOF-1,[48,49,55] M-IRMOF-10,[50] M-IRMOF-14,[51] M-IRMOF-993,[52] (M = Zn, Cd, alkaline earth metals), $M_4O(FMA)_3$ (M=Zn and Cd),[56] and A-IRMOF-M0,[53] (A = Zn, Cd, alkaline earth metals) series.

If one considers changing just the metal atoms in each of the *M*-UiO-66, -67, -68 sub-series, then each set has the same linkers and similar nodes. Although these tetravalent

metals in this series have different atomic numbers and atomic or ionic radii, they have the same valence shell electron configurations. The HOCO - LUCO gaps for the Ti-UiO series are consistently the lowest. The replacement of divalent Zn ions in IRMOF-1, -10, -14, -993 with divalent alkaline-earth metal ions gives similar electronic structure and bonding behavior. The isoelectronic nature of the compounds within this series contributes to the similar TDOS patterns (**Fig. 4**) and also the trending band gap values.

## E. Chemical Bonding

### i. Partial density of states (PDOS):

We focus on the experimentally accessible Zr-UiO-66, and then extend our discussion to the other materials. We expect that the chemical bonding should be very similar for UiO-66, 67, 68, as the linkers are extended in length. This has already been demonstrated in a series of work on IRMOFs from our group.[48-52] We will discuss the general trends for the whole series.

From the PDOS of Zr-UiO-66 in **Fig. 3**, one can characterize the distribution of various electronic states in the valence band and the conduction band. The *d*-states of Zr atoms are primarily contributing to the conduction band (CB), whereas the *s*-states of H atoms are primarily contributing to the valence band (VB). Both *s*- and *p*-states of C and O atoms also contribute significantly to the VB. Both *s*- and *p*-states of C1 and C2, C2 and C3, C3 and O1 are distributed energetically in the same range, moreover, they are spatially adjacent to each other (see **Fig. 1.** or **Scheme S1.** for the atomic arrangement in the bulk framework), and thus their valence band states can effectively overlap and form very strong covalent bonds. This is consistent with the following analysis of the electron localization function plot, i.e., the ELF values between C1 and C2, C2 and C3, C3 and O1 are higher than that between other C-atoms. The *s*-states of H1 can overlap with the *p*-states of O3 in the energy range between −8.0 to −5.0 eV and can form covalent bonds. The *s*-states of H2 can overlap with the *p*-states of C1 in the energy range between −10 to −2.5 eV and can form covalent bonds. The *p*-state of C3 can overlap with that of O1 in the energy range between −7.5 to −2.5 eV and form a directional bond between them. The *d*-state of Zr is well localized, and also the Zr *s*-electrons are transferred to the neighboring atoms, which leads to ionic bonding between Zr and O. This is also consistent with the following analysis of charge density and ELF.

The chemical bonding for the other systems M-UiO-66 to 68 (M = Ti, Zr, and Hf) is similar to that of Zr-UiO-66. Specifically, the chemical bonding of C, H, and O atoms are almost identical to that of Zr-UiO-66. In general, the chemical bonding between M and O is

mainly ionic together with some covalency. The difference of chemical bonding comes from the different ratio between ionicity and covalency between different M-O bonds, e.g., there is more covalency and less ionicity in the Ti-O bond compared to Hf-O, even though both have mainly ionic components. This is consistent with the results from the following bond overlap population (BOP)/Hirshfeld charge analyses.

**ii. Charge density, charge transfer, and ELF analyses:**

To further improve the understanding of the bonding interactions, we turn our attention to charge density/transfer, ELF, and bond overlap population (BOP)/Mulliken population analyses. Perspective plots in (a) side view, (b) tilted side view, (c) top view of the UiO-66 framework are shown in **Scheme S3** to aid in understanding the chemical bonding. One can see the distribution of different atoms in the same planes, above or below the planes, and the different spatial positions in the frameworks.

We plot the charge density, charge transfer, and electron localization function in the [001] plane. In **Fig. 1d** one can see the spatial distribution of different atoms in the bulk framework. The detailed plot is shown in **Fig. 6a**, from which we can see that one linker connected by two nodes. In the node, we can see that there are six Zr-atoms, but they are not coplanar. The outer four Zr-atoms located coplanar with the linker BDC, the central two are located above and below that plane. Moreover, the four O-atoms connected by Zr-atoms are located below the planar. From **Fig. 6a**, we can see that there is low charge density distributed on the sites of Zr-atoms. The charge density was transferred from Zr to O.

From **Fig. 1d** and **Fig. 6a**, it is clear that C, H, and O atoms in the organic linker form a molecule-like structural subunit $O_2C$-$C_6H_4$-$CO_2$ (BDC). As a result, the C-C, C-H, and C-O bonding interactions are dominantly covalent in character. Moreover, there is substantial charge density distributed between C atoms, and between C and H and O atoms in the $O_2C$-$C_6H_4$-$CO_2$ subunits. This substantiates the presence of covalent bonding like that in organic molecules. From **Fig. 6a**, it can be seen that the charges are spherically distributed at the M and O sites, which is characteristic for systems having ionic interactions. Additionally, there is no noticeable charge density distributed between M and O atoms which clearly demonstrate the presence of ionic bonding.

The same BDC linker is found in MOF-5, however, with a different topology[48]. For MOF-5, the node (metal cluster $Zn_4O$) is six fold coordinated by organic BDC linkers, whereas for UiO-66, the node (metal cluster $Zr_6O_4(OH)_4$) is twelve coordinated by organic linker.

For the O atoms in the linker BDC, we can see that the maximum charge density is located at the O sites. On the other hand, there is less charge density distributed on those O atoms connected by Zr since the plane we used to plot this figure does not cross the maximum charge density of those O atoms, as these atoms are located out of the plane.

Another convenient and illustrative way to represent and analyze the bonding effects in Zr-UiO-66 is to use charge transfer plots. The charge-transfer contour is the self-consistent electron density in a particular plane, $\rho_{comp}$, minus the electron density of the overlapping free atoms in the same lattice, $\rho_{atom.}$, i.e., $\Delta\rho(r) = \rho_{comp.} - \rho_{atom.}$, which allows one to visualize how electrons are redistributed in a particular plane compared to free atoms due to the bonding in the compound. From **Fig. 6b**, it is clear that electrons are transferred from Zr to O sites. But the charge transfer from Zr is not isotropic as clearly seen from **Fig. 6a**. The anisotropic charge transfer from Zr to the O sites indicates the presence of iono-covalent bonding between Zr and O. But the ionic bonding interaction dominates over the covalent interaction between Zr and O. Furthermore, electron densities from the C, O, and H atoms are transferred to the regions in between these atoms, and the nonspherical electron distribution clearly indicates the presence of strong covalent bonding. From **Fig. 6c**, it can be inferred that the large value of ELF at the O site indicates strongly paired electrons with local bosonic character. The negligibly small ELF between Zr and O, and the small value of ELF at the Zr site (partially due to the presence of *d* electrons for the transition metals Zr) with spherically symmetric distribution indicate that the bonding interaction between Zr and O is dominated by an ionic interaction. The ELF distribution at the O site is not spherically symmetric and it is polarized towards the Zr atoms, indicating the presence of directional bonding between Zr and O. A certain polarized character is found in the ELF distribution at the H sites in Zr-UiO-66 indicating the presence of polar covalent bonding. There is a maximum in the ELF between the C atoms and between C and O, indicating covalent bonds. From the above analyses, one can identify the chemical bonding in Zr-UiO-66. This bonding will be similar for Zr-UiO-67, and 68.

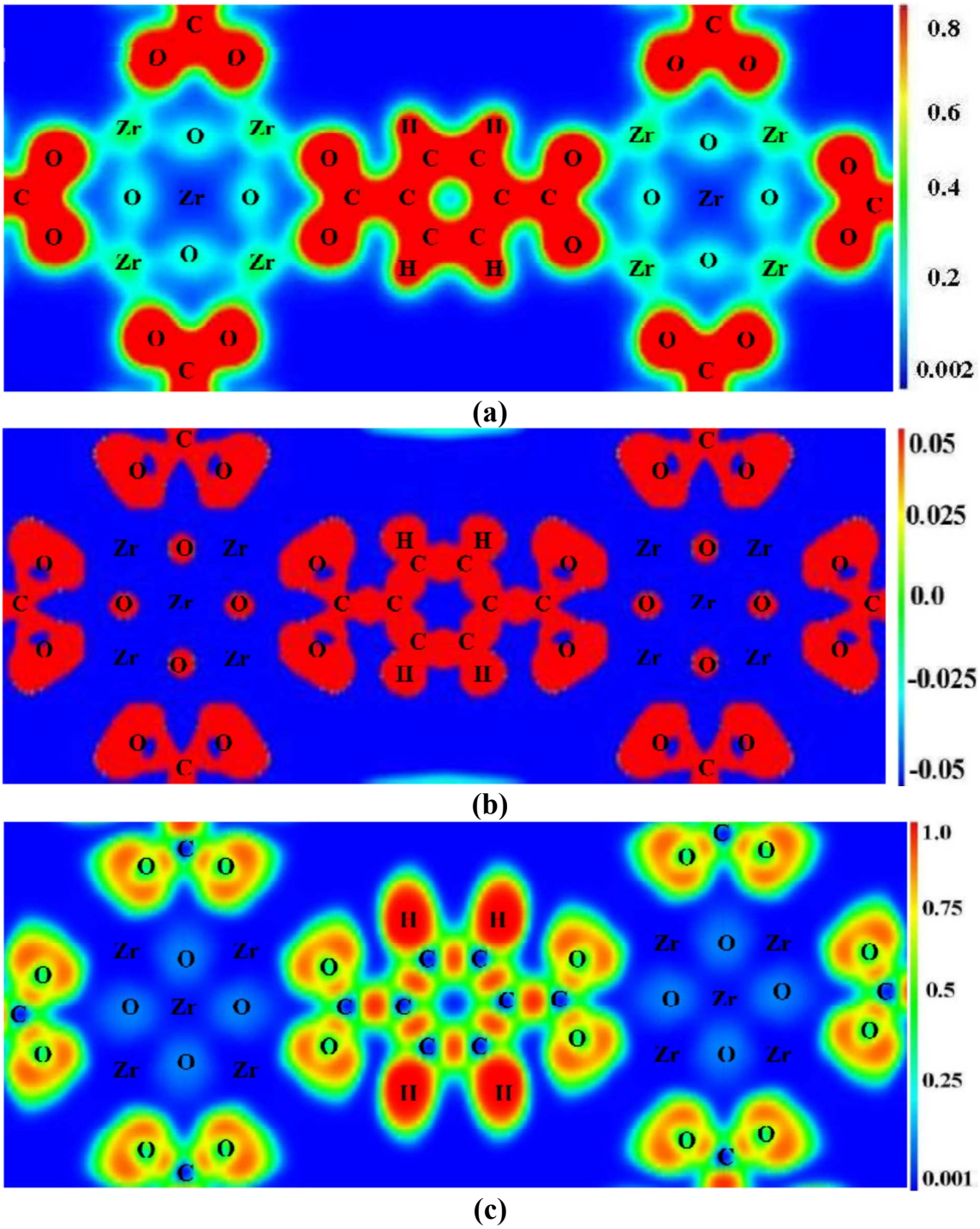


**Figure 6. (a)** Calculated charge density plot, **(b)** charge transfer plot, and **(c)** electron localization function plot for Zr-UiO-66 for the (110) plane.

**iii. Hirshfeld charge and bond overlap population analysis**

On the basis of a recent evaluation of different charge density analysis tools, the Hirshfeld charge is more reliable than the other types of methods for charge analysis that were available

in VASP and materials studio (e.g., Mulliken, Bader, Weinhold).[73] Therefore, we will use the Hirshfeld charge for the current systems.

The calculated Hirshfeld charges (HC) are reported in **Table S3** for M-UiO-66 and -68 (M = Ti, Zr, and Hf) series. The corresponding HC values on the metal atom M are +0.52 |e| for Ti, +0.64 |e| for Zr, and Hf. Note that the charge distribution on the metal atoms are much smaller than that of formal oxide states (+4). In organic linkers, the C1 atoms (in UiO-66) connected to H2 bear negative charges (–0.03|e|). The C4, C5, and C6 atoms (in UiO-68) connected to H atoms bear negative charges (–0.04|e|). However, the C2 atoms (in UiO-66), C2, C3, and C7 atoms (in UiO-68) bonded to C bear nearly zero charge. But, the C3 atoms (in UiO-66) connected to O1 (in UiO-66) bear positive charge +0.2|e|. The C1 atoms (in UiO-68) connected to O3 (in UiO-68) bear positive charge (+0.19|e|). The situation is identical in both UiO-66 and -68.

Finally, we classified oxygen atoms into three types, i.e., O1, O2, and O3. For M-UiO-66, O1 atom, with –0.18 ~ –0.20|e| charges, is the oxygen atom of carboxylate (–$CO_2$); O2 atom, with the largest negative charges (–0.28 ~ –0.34|e|), is the oxygen atom in the node (metal cluster) without proton on it; the last one O3, with –0.22 ~ –0.25|e| charges, is the atom with proton on it in the node. The situation is very similar to that of M-UiO-68, but still with some difference due to different numbering of O atoms. In detail, the O1 atom in M-UiO-68, similar to that of O3 in M-UiO-66, with the largest negative charges (–0.22 ~ –0.25|e|), is the atom with proton on it in the node. The O2 atom in M-UiO-68, very similar to (equivalent) that of O2 in M-UiO-66, baring the largest negative charges (–0.28 ~ –0.34|e|), is the oxygen atom in the node without proton on it. The O3 atom in M-UiO-68, similar to O1 in M-UiO-66, baring –0.18 ~ –0.20|e| charges, is the oxygen atom of carboxylate (–$CO_2$).

Even if this analysis tends to overestimate covalence contributions in chemical bonding, it provides reasonable trends, especially for comparisons between similar species (UiO-66 and UiO-68) as it is the case in the present work. The results are very similar for both MOFs, showing in both cases a central titanium with a charge ~ +0.5 and the oxygen significantly negative (–0.2 ~ –0.3).

In summary, the Hirshfeld charge analysis provides a picture of the M-O bond corresponding to a significant deviation from a purely ionic interaction [i.e., M(IV) and O(II)].

In order to have a better understanding about the interaction between the constituents, the bond overlap population (BOP) values are calculated. The BOP can provide useful information about the bonding property between the two atoms. A high BOP value indicates a

strong covalent bond, while a low BOP value indicates an ionic/nonbonding interaction. The calculated BOP values for the M-O, C-O, C-C, and C-H bonds are displayed in **Table S3**. From **Table S3** it can be seen that the BOP values for the M-O bonds in the crystal varies in the range 0.17-0.32 for M = Ti, 0.17-0.33 for Zr, and 0.22-0.45 for Hf, respectively, which indicates a dominantly ionic character. The order of covalent component in the M-O bonds is Ti-O $\approx$ Zr-O > Hf-O, which is consistent with the general trend of the atomic properties within the same group. Similarly, the calculated BOP values for the C-O bond are in the range 0.93-0.94, which is very close to a covalent C-O single bond. The BOP values are in the range 0.88-0.90, indicative of covalent character. For the C-C bonds, the calculated BOP values vary between 0.84 and 1.14, the latter of which is comparable to the covalent C-C bond in diamond (1.08), and therefore, the C-C bonds are strong covalent bonds. Therefore, the M-O bonds in the nodes of M-UiO-66, 67, 68 have predominant ionic character similar to that present in $MO_2$, whereas the C-H, C-O and C-C bonds in the linkers have covalent interactions such as those in regular organic molecules.

The above discussions demonstrated by that analyses based on charge density/transfer, ELF, Hirshfeld charge, and bond overlap population (BOP) analyses give a consistent view of the chemical bonding in M-UiO-66, 67, 68 (M = Ti, Zr, and Hf) series. From the above analysis, we can see that the situation of chemical bonding similar for each material within M-UiO-66, 67, 68 series, and is also similar to that of M-IRMOF-1,[48,49] M-IRMOF-10,[50] M-IRMOF-14,[51] M-IRMOF-993,[52] (M = Zn, Cd, alkaline earth metals), and A-IRMOF-M0,[53] (A = Zn, Cd, alkaline earth metals) series and $M_4O(FMA)_3$,[56] (M=Zn, Cd) in our recent series work.

### F. Band structures and optical properties

The conversion of solar energy into hydrogen by a splitting process assisted by semiconductor photocatalysts is a promising way to produce renewable hydrogen. The calculations in this paper show that M-UiO-66, 67, 68 have HOCO - LUCO gaps ranging from 2.9 to 4.1 eV, and have potential applications for hydrogen photocatalysis. More excitingly, recent experiments have already shown that Zr-UiO-66 and Zr-UiO-66-$NH_2$ can be used as photocatalysts for hydrogen generation[10] in methanol or water/methanol, which triggers great interest in the optical properties of Zr-UiO-66 and analogues. Doped UiO-67 materials have also been used for catalytic water oxidation, carbon dioxide reduction, and organic photocatalysis. This combination of molecular catalysts and UiO materials

demonstrates potential for development of highly active heterogeneous catalysts for solar energy utilization.[74] These UiO materials are tough and resistant to water and methanol, which makes them well suited to these applications. Moreover, with a novel and unique typology for MOFs, these materials may have new and unexpected applications. The optical properties for UiO-66, 67, 68 are of interest, for example, in view of potential uses of this material in hybrid solar cell applications as an active material or in the buffer layer between the electrodes and inorganic active materials. Additionally, as novel arene-based materials, the UiO materials may have potential applications in organic semiconducting devices such as field-effect transistors, solar cells, and organic light-emitting devices (OLEDs). In the **SI**, we also present the optical properties of Zr-UiO-68, Hf-UiO-66, -68, and Ti-UiO-66, -68. Below, we focus on the experimentally available Zr-UiO-66.

The UiO-series are typical cases to demonstrate the tunability of band gap and optical response properties, for example, increase in conjugation of an organic linker or using an electron donor substituted arene will give a bathochromic shift in absorption maxima. This phenomenon is well illustrated in the UV-Vis spectra reported for a series of isostructural UiOs-66/67.[22]

The central quantity of the optical properties is the dielectric function $\varepsilon(\omega)$, which describes the linear response of the system to electromagnetic radiation. Here $\varepsilon(\omega)$ is connected with the interaction of photons with electrons. Its imaginary part $\varepsilon_2(\omega)$ can be derived from interband optical transitions by calculating the momentum matrix elements between the occupied and unoccupied wave functions within the selection rules, and its real part $\varepsilon_1(\omega)$ can be derived from $\varepsilon_2(\omega)$ by the Kramer-Kronig relationship.[75] The real part of $\varepsilon(\omega)$ in the limit of zero energy (or infinite wavelength) is equal to the square of the refractive index $n$. All the frequency dependent linear optical properties, such as refractive index $n(\omega)$, extinction coefficient $k(\omega)$, absorption coefficient $\alpha(\omega)$, optical conductivity $\sigma(\omega)$, reflectivity $R(\omega)$ and electron energy-loss spectrum $L(\omega)$ can be deduced from $\varepsilon_1(\omega)$ and $\varepsilon_2(\omega)$.[75]

We have performed CASTEP calculations to estimate the optical response properties of Zr-UiO-66 and the results from the optical calculations are shown in **Fig. 7**. The calculated optical properties have been shifted by the scissor operator based on the experimental band gap (4.07 eV) of Zr-UiO-66. A similar correction has also been applied to the calculated optical properties of other materials within UiO-series.

Five sharp peaks together with some shallow peaks constitute the main character of $\varepsilon_2(\omega)$ (**Fig**. **7a**) of Zr-UiO-66. In the following discussion, we focus on the major sharp peaks, at 5.2, 6.7, 8.9, 15.1, and 33.7 eV. The real part of dielectric function $\varepsilon_1(\omega)$ (**Fig**. **7a**) ($\varepsilon_1(0)$=2.2)

allows us to estimate the value of the refractive index $n(\omega)$ at infinite wavelength $n(0)$=1.5 for Zr-UiO-66. At low frequency, the imaginary part $\varepsilon_2(\omega)$ is zero and this is consistent with the band gap of Zr-UiO-66. At higher frequency (> 45 eV), the imaginary part $\varepsilon_2(\omega)$ approaches zero.

The reflectivity spectrum (**Fig**. **7b**) of Zr-UiO-66 shows five sharp and strong peaks at 5.1, 6.7, 8.9, 15.3, and 34.1 eV. A broad peak composed of twin peaks can be found at 18.2 and 19.1 eV. Several other peaks can be found at 10.9, 10.9, 16.5, 22.8, 22.8, 32.2, 35.8 eV. The two peaks at 4.4 and 5.9 eV, in the low energy range, mainly arise from the C (2p) → O (2p) as well as Zr (4d) → C/O (2p) interband transitions. The reflectivity approaches zero when the frequency exceeds 50 eV for Zr-UiO-66. The value of reflectivity is 0.039 (i.e., $R(0)$) for Zr-UiO-66. Overall, the calculated reflectivity in the whole frequency range is much smaller than that in inorganic solids, e.g., the corresponding metal oxides $ZrO_2$. This may be one of the advantageous optical properties of these materials for use in optoelectronic devices (such as solar cells and LEDs) where one may want low reflectivity.

Zr-UiO-66 has a refractive index $n(\omega)$ (**Fig**. **7c**) in the range 4.1 to 40 eV, and no refractive index in the energy regions lower than 4.07 eV or higher than 40 eV. This is consistent with the band gap of Zr-UiO-66. The extinction coefficient $k(\omega)$ (the imaginary part of the complex refractive index) (**Fig**. **7c**) of Zr-UiO-66 shows five sharp peaks at 5.3, 6.8, 8.9, and 15.3 eV. Another sharp peak can be seen at 33.8 eV in the high energy region.

The optical conductivity $\sigma(\omega)$ plot of Zr-UiO-66 is shown in **Fig**. **7d**. The real part of the complex conductivity has five major sharp peaks at 5.3, 6.7, 8.9, 15.2, and 33.7 eV. Several other shallow peaks located at 11.3, 16.3, 17.9, 22.3, 32.0, and 35.4 eV.

The electron energy-loss function $L(\omega)$ (**Fig**. **7e**) is an important optical parameter describing the energy loss of a fast electron traversing a certain material. The peaks in the $L(\omega)$ spectra represent the characteristics associated with the plasma resonance and the corresponding frequency is called plasma frequency above which the material is a dielectric [$\varepsilon_1(\omega) > 0$] and below which the material behaves like a metallic compound in some sense [$\varepsilon_1(\omega) < 0$]. In addition, the peaks of the $L(\omega)$ spectra overlap the trailing edges in the reflectivity spectra. In the low energy range, there are three sharp peaks located at 5.6, 7.1, and 9.5 eV. Followed by two shallow peaks located at 11.1 and 17.1 eV. Then, two sharp peaks at 19.8 and 23.2 eV. In the higher energy range, there is a very sharp and intense peak located at 34.1 eV, followed by two sharp shoulders at 32.1 and 35.5 eV on the left and right sides, respectively. In general, the shape and main peaks of $L(\omega)$ is quite similar to that of absorption spectrum $\alpha(\omega)$ ($cm^{-1}$).

Zr-UiO-66 has an absorption band (**Fig**. **7f**) from 4.07 to 50 eV. Three strong and sharp peaks at 5.3, 6.8, and 9.1 eV, followed by a shallow shoulder at about 11.3 eV. The strongest peak can be found at 15.4 eV, followed by another sharp peak at 16.5 eV. A broad peak consists of twin peaks located at 18.1 and 18.8 eV, followed by sharp peaks at 22.5 and 33.8 eV.

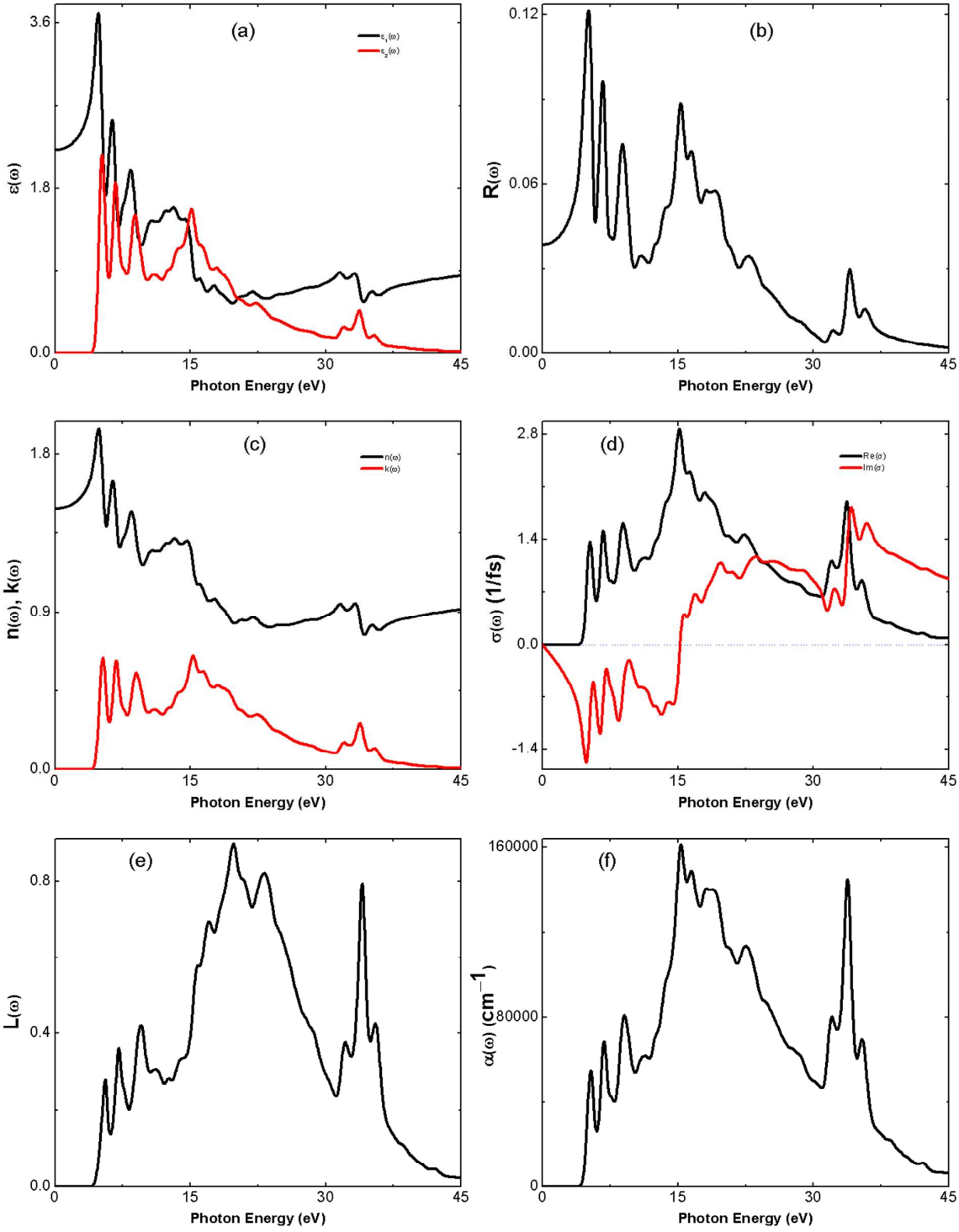

**Figure 7.** The calculated optical spectra for Zr-UiO-66: (a) dielectric function ε(ω); (b) reflectivity R(ω); (c) refractive index **n**(ω) and extinction coefficient **k**(ω); (d) optical conductivity σ(ω); (e) energy loss function L(ω); and (f) absorption coefficient α(ω) ($cm^{-1}$).

In parallel with the optical properties calculations we have also calculated the band structures of the M-UiO-66 and -68 (M = Ti, Zr, and Hf) series. The calculated results can be found in the **SI**. From **Figs**. **S24-S29**, we can see that this is a direct bandgap material. Unlike typical metal-organic framework materials,[48-52] these materials does not have flat bands. This suggests the possibility that this material could be doped to increase the conductivity for use in applications.

## IV. Conclusions

We have presented a comprehensive investigation on the ground state structure, formation enthalpies, electronic structure, chemical bonding, and optical properties of experimentally synthesized Zr-UiO-66, 67, 68 and Hf-UiO-66 and analogues M-UiO-66, 67, 68 (M = Ti and Hf).

(1) The calculations show that the values of bulk modulus range from 15 to 38 GPa, indicating that each material is relatively "soft". However, they are more "rigid" than prototypical MOF-5. The optimized atomic positions and lattice parameters of Zr-UiO-66, -67, and -68 are generally comparable to the experimental results. We find that the combination of experimental and computational results together lead to a fuller understanding of these complicated MOF crystal structures. We predicted that Hf can be substituted for Zr in the UiO structures, and this has been realized experimentally in Hf-UiO-66. We presented optimized structures and lattice constants for the remaining Hf-UiO-67, 68. We also predict that Ti can be substituted into the UiO-66, 67, 68 and found a smaller lattice constant.

(2) The large negative formation enthalpy of all of these UiO materials is consistent with the fact that four of them have already been synthesized, and also indicates that the novel materials Ti-UiO-66, 67, 68 and Hf- UiO-67, 68 are highly stable and could be experimentally synthesized.

(3) Electronic charge density, charge transfer, and ELF analyses shed light on the character of the chemical bonds between M-O, C-O, C-H, and C-C in the UiO series. The bonding interaction between M-O is mainly an ionic interaction, whereas those between C-O, C-H, and C-C are mainly covalent interactions. Moving from Ti to Hf, the ionicity decreases and the covalency increases in the M-O bonds.

(4) The M-UiO-66, 67, 68 series have HOCO - LUCO gaps ranging from 2.9 to 4.1 eV.

The gap can be tuned by varying the linkers. These materials may be useful as photocatalysts. We hope that this study will trigger further research in the synthesis of optically active MOFs with targeted bandgaps for applications in optoelectronic devices.

(5) The calculated optical properties of the M-UiO-66, 67, 68 series provide useful information for future experimental exploration. For example, the reflectivity and maximum absorption coefficient of UiO-66 are only 10% and 30% of that of corresponding oxide $ZrO_2$, respectively. This may be useful in optoelectronic devices such as solar cells and LEDs where low reflectivity can be desirable. Additionally, it might provide information for the potential uses of this material in hybrid solar cell applications as an active material or in the buffer layer between the electrodes and inorganic active materials. Unlike typical metal-organic framework materials, these materials do not have flat bands. Finally, these materials may have potential applications in organic semiconducting devices such as field-effect transistors, solar cells, and organic light-emitting devices (OLEDs).

**Acknowledgements**

We gratefully acknowledge the financial support by the Research Council of Norway through a Centre of Excellence Grant (Grant No. 179568/V30) and the Norwegian Supercomputing Program (NOTUR) through a grant of computer time (Grant No. NN4654K). We also thank the Minnesota Supercomputer Institute for support.

**Supporting Information Available:** The plots of PXRD, TDOS, PDOS, charge density, charge transfer, ELF, the band structures and optical properties and the calculated Hirshfeld charge (HC), Mulliken effective charge (MEC), bond overlap populations (BOP) for M-UiO-66, 67, 68 (M = Ti, Zr, and Hf) series can be found in the supporting information.

## References


(1) *Chem. Soc. Rev.* **2009**, *38 (5)*, 1201~1508 Special Issue on MOFs.

(2) *Chem. Rev.* **2012**, *112 (2)*, 673~1268 Special Issue on MOFs.

(3) Jeffrey R. Long; Omar M. Yaghi *Chem. Soc. Rev.* **2009**, *38*, 1213.

(4) Chui, S. S. Y.; Lo, S. M. F.; Charmant, J. P. H.; Orpen, A. G.; Williams, I. D. *Science* **1999**, *283*, 1148.

(5) Li, H.; Eddaoudi, M.; O'Keeffe, M.; Yaghi, O. M. *Nature* **1999**, *402*, 276.

(6) Ockwig, N. W.; Delgado-Friedrichs, O.; O'Keeffe, M.; Yaghi, O. M. *Acc. Chem. Res.* **2005**, *38*, 176.

(7) Surble, S.; Serre, C.; Mellot-Draznieks, C.; Millange, F.; Ferey, G. *Chem. Commun.* **2006**, 284.

(8) Cavka, J. H.; Jakobsen, S.; Olsbye, U.; Guillou, N.; Lamberti, C.; Bordiga, S.; Lillerud, K. P. *J. Am. Chem. Soc.* **2008**, *130*, 13850.

(9) Valenzano, L.; Civalleri, B.; Chavan, S.; Bordiga, S.; Nilsen, M. H.; Jakobsen, S.; Lillerud, K. P.; Lamberti, C. *Chem. Mater.* **2011**, *23*, 1700.

(10) Silva, C. G.; Luz, I.; Llabres i Xamena, F. X.; Corma, A.; Garcia, H. *Chem. Eur. J.* **2010**, *16*, 11133.

(11) Abid, H. R.; Pham, G. H.; Ang, H.-M.; Tade, M. O.; Wang, S. *J. Colloid Interface Sci.* **2012**, *366*, 120.

(12) Guillerm, V.; Gross, S.; Serre, C.; Devic, T.; Bauer, M.; Ferey, G. *Chem. Commun.* **2010**, *46*, 767.

(13) Chavan, S.; Vitillo, J. G.; Uddin, M. J.; Bonino, F.; Lamberti, C.; Groppo, E.; Lillerud, K.-P.; Bordiga, S. *Chem. Mater.* **2010**, *22*, 4602.

(14) Yang, Q.; Wiersum, A. D.; Llewellyn, P. L.; Guillerm, V.; Serred, C.; Maurin, G. *Chem. Commun.* **2011**, *47*, 9603.

(15) Yang, Q.; Jobic, H.; Salles, F.; Kolokolov, D.; Guillerm, V.; Serre, C.; Maurin, G. *Chem. Eur. J.* **2011**, *17*, 8882.

(16) Yang, Q.; Wiersum, A. D.; Jobic, H.; Guillerm, V.; Serre, C.; Llewellyn, P. L.; Maurin, G. *J. Phys. Chem. C* **2011**, *115*, 13768.

(17) Barcia, P. S.; Guimaraes, D.; Mendes, P. A. P.; Silva, J. A. C.; Guillerm, V.; Chevreau, H.; Serre, C.; Rodrigues, A. E. *Microporous Mesoporous Mater.* **2011**, *139*, 67.

(18) Schaate, A.; Roy, P.; Godt, A.; Lippke, J.; Waltz, F.; Wiebcke, M.; Behrens, P. *Chem. Eur. J.* **2011**, *17*, 6643.

(19) Kandiah, M.; Usseglio, S.; Svelle, S.; Olsbye, U.; Lillerud, K. P.; Tilset, M. *J. Mater. Chem.* **2010**, *20*, 9848.

(20) Kandiah, M.; Nilsen, M. H.; Usseglio, S.; Jakobsen, S.; Olsbye, U.; Tilset, M.; Larabi, C.; Quadrelli, E. A.; Bonino, F.; Lillerud, K. P. *Chem. Mater.* **2010**, *22*, 6632.

(21) Garibay, S. J.; Cohen, S. M. *Chem. Commun.* **2010**, *46*, 7700.

(22) Chavan, S.; Vitillo, J. G.; Gianolio, D.; Zavorotynska, O.; Civalleri, B.; Jakobsen, S.; Nilsen, M. H.; Valenzano, L.; Lamberti, C.; Lillerud, K. P.; Bordiga, S. *Phys. Chem. Chem. Phys.* **2012**, *14*, 1614.

(23) Schaate, A.; Roy, P.; Preusse, T.; Lohmeier, S. J.; Godt, A.; Behrens, P. *Chem. Eur. J.* **2011**, *17*, 9320.

(24) Gianolio, D.; Vitillo, J. G.; Civalleri, B.; Bordiga, S.; Olsbye, U.; Lillerud, K. P.; Valenzano, L.; Lamberti, C. *J. Phys. Conf. Ser.* **2013**, *430*, 012134.

(25) Jakobsen, S.; Gianolio, D.; Wragg, D. S.; Nilsen, M. H.; Emerich, H.; Bordiga, S.; Lamberti, C.; Olsbye, U.; Tilset, M.; Lillerud, K. P. *Phys. Rev. B* **2012**, *86*, 125429.

(26) Xydias, P.; Spanopoulos, I.; Klontzas, E.; Froudakis, G. E.; Trikalitis, P. N. *Inorg. Chem.* **2013**, *53*, 679.

(27) Wu, H.; Yildirim, T.; Zhou, W. *J. Phys. Chem. Lett.* **2013**, *4*, 925.

(28) Vermoortele, F.; Bueken, B.; Le Bars, G.; Van de Voorde, B.; Vandichel, M.; Houthoofd, K.; Vimont, A.; Daturi, M.; Waroquier, M.; Van Speybroeck, V.; Kirschhock, C.; De Vos, D. E. *J. Am. Chem. Soc.* **2013**, *135*, 11465.

(29) Ragon, F.; Horcajada, P.; Chevreau, H.; Hwang, Y. K.; Lee, U. H.; Miller, S. R.; Devic, T.; Chang, J.-S.; Serre, C. *Inorg. Chem.* **2014**, *53*, 2491.

(30) Falkowski, J. M.; Sawano, T.; Zhang, T.; Tsun, G.; Chen, Y.; Lockard, J. V.; Lin, W. *J. Am. Chem. Soc.* **2014**, *136*, 5213.

(31) Feng, D.; Chung, W.-C.; Wei, Z.; Gu, Z.-Y.; Jiang, H.-L.; Chen, Y.-P.; Darensbourg, D. J.; Zhou, H.-C. *J. Am. Chem. Soc.* **2013**, *135*, 17105.

(32) He, C.; Lu, K.; Liu, D.; Lin, W. *J. Am. Chem. Soc.* **2014**, *136*, 5181.

(33) Kresse, G.; Hafner, J. *Phys. Rev. B* **1993**, *47*, 558.

(34) Kresse, G.; Hafner, J. *Phys. Rev. B* **1994**, *49*, 14251.

(35) Kresse, G.; Furthmuller, J. *Phys. Rev. B* **1996**, *54*, 11169.

(36) Kresse, G.; Furthmuller, J. *Comput. Mater. Sci.* **1996**, *6*, 15.

(37) Segall, M. D.; Lindan, P. J. D.; Probert, M. J.; Pickard, C. J.; Hasnip, P. J.; Clark, S. J.; Payne, M. C. *J. Phys.: Condens. Matter* **2002**, *14*, 2717.

(38) *Materials Studio, ver. 5.0, Accelrys, San Diego, CA, 2009.*

(39) Perdew, J. P. In *Electronic Structure of Solids 1991*; Ziesche, P., Eschrig, H., Eds.; Akademie Verlag: Berlin, 1991, p 11.
(40) Perdew, J. P.; Burke, K.; Wang, Y. *Phys. Rev. B: Condens. Matter* **1996**, *54*, 16533.
(41) Perdew, J. P.; Burke, K.; Ernzerhof, M. *Phys. Rev. Lett.* **1996**, *77*, 3865.
(42) Kresse, G.; Joubert, D. *Phys. Rev. B: Condens. Matter* **1999**, *59*, 1758.
(43) Blöchl, P. E. *Phys. Rev. B: Condens. Matter* **1994**, *50*, 17953.
(44) Becke, A. D.; Edgecombe, K. E. *J. Chem. Phys.* **1990**, *92*, 5397.
(45) Savin, A.; Becke, A. D.; Flad, J.; Nesper, R.; Preuss, H.; von Schnering, H. G. *Angew. Chem., Int. Ed. Engl.* **1991**, *30*, 409.
(46) Savin, A.; Jepsen, O.; Flad, J.; Andersen, O. K.; Preuss, H.; von Schnering, H. G. *Angew. Chem., Int. Ed. Engl.* **1992**, *31*, 187.
(47) Silvi, B.; Savin, A. *Nature* **1994**, *371*, 683.
(48) Yang, L.-M.; Vajeeston, P.; Ravindran, P.; Fjellvag, H.; Tilset, M. *Inorg. Chem.* **2010**, *49*, 10283.
(49) Yang, L.-M.; Vajeeston, P.; Ravindran, P.; Fjellvag, H.; Tilset, M. *Phys. Chem. Chem. Phys.* **2011**, *13*, 10191.
(50) Yang, L. M.; Ravindran, P.; Vajeeston, P.; Tilset, M. *RSC Adv.* **2012**, *2*, 1618.
(51) Yang, L. M.; Ravindran, P.; Vajeeston, P.; Tilset, M. *Phys. Chem. Chem. Phys.* **2012**, *14*, 4713.
(52) Yang, L. M.; Ravindran, P.; Vajeeston, P.; Tilset, M. *J. Mater. Chem.* **2012**, *22*, 16324.
(53) Yang, L.-M. *Microporous Mesoporous Mater.* **2014**, *183*, 218.
(54) Yang, L.-M.; Pushpa, R. *J. Mater. Chem. C* **2014**, *2*, 2404.
(55) Yang, L.-M.; Ravindran, P.; Vajeeston, P.; Svelle, S.; Tilset, M. *Microporous Mesoporous Mater.* **2013**, *175*, 50.
(56) Yang, L.-M.; Ravindran, P.; Tilset, M. *Inorg. Chem.* **2013**, *52*, 4217.
(57) Yang, L.-M.; Fang, G.-Y.; Ma, J.; Ganz, E.; Han, S. S. *Cryst. Growth Des.* **2014**, *14*, 2532.
(58) Birch, F. *Phys. Rev.* **1947**, *71*, 809.
(59) Cotton, F. A.; Wilkinson, G.; Murillo, C. A.; Bochmann, M. In *Advanced Inorganic Chemistry*; Wiley: New York, 2000.
(60) deKrafft, K. E.; Boyle, W. S.; Burk, L. M.; Zhou, O. Z.; Lin, W. *J. Mater. Chem.* **2012**, *22*, 18139.
(61) Dan-Hardi, M.; Serre, C.; Frot, T.; Rozes, L.; Maurin, G.; Sanchez, C.; Ferey, G. *J. Am. Chem. Soc.* **2009**, *131*, 10857.
(62) Fu, Y.; Sun, D.; Chen, Y.; Huang, R.; Ding, Z.; Fu, X.; Li, Z. *Angew. Chem. Int. Ed.* **2012**, *51*, 3364.
(63) Baranwal, B. P.; Singh, A. K.; Varma, A.; Pandey, A. C. *Synthesis and Reactivity in Inorganic Metal-Organic and Nano-Metal Chemistry* **2011**, *41*, 150.
(64) Frot, T.; Cochet, S.; Laurent, G.; Sassoye, C.; Popall, M.; Sanchez, C.; Rozes, L. *Eur. J. Inorg. Chem.* **2010**, 5650.
(65) Cho, D.; Bae, W. J.; Joo, Y. L.; Ober, C. K.; Frey, M. W. *J. Phys. Chem. C* **2011**, *115*, 5535.
(66) Perdew, J. P.; Levy, M. *Phys. Rev. Lett.* **1983**, *51*, 1884.
(67) Levine, Z. H.; Allan, D. C. *Phys. Rev. B: Condens. Matter* **1991**, *43*, 4187.
(68) Fahmi, A.; Minot, C.; Silvi, B.; Causa, M. *Phys. Rev. B* **1993**, *47*, 11717.
(69) Mo, S. D.; Ching, W. Y. *Phys. Rev. B* **1995**, *51*, 13023.
(70) Asahi, R.; Taga, Y.; Mannstadt, W.; Freeman, A. J. *Phys. Rev. B* **2000**, *61*, 7459.
(71) Chen, Q.; Cao, H. H. *Chin. Phys.* **2004**, *13*, 2121.
(72) Feng, P. L.; Perry Iv, J. J.; Nikodemski, S.; Jacobs, B. W.; Meek, S. T.; Allendorf, M. D. *J. Am. Chem. Soc.* **2010**, *132*, 15487.
(73) Guerra, C. F.; Handgraaf, J.-W.; Baerends, E. J.; Bickelhaupt, F. M. *J. Comput. Chem.* **2004**, *25*, 189.
(74) Wang, C.; Xie, Z.; deKrafft, K. E.; Lin, W. *J. Am. Chem. Soc.* **2011**, *133*, 13445.
(75) Yu, P. Y.; Cardona, M. In *Fundamentals of Semiconductors* Springer-Verlag: Berlin, 1996.

## Table of Contents Synopsis and Graphic

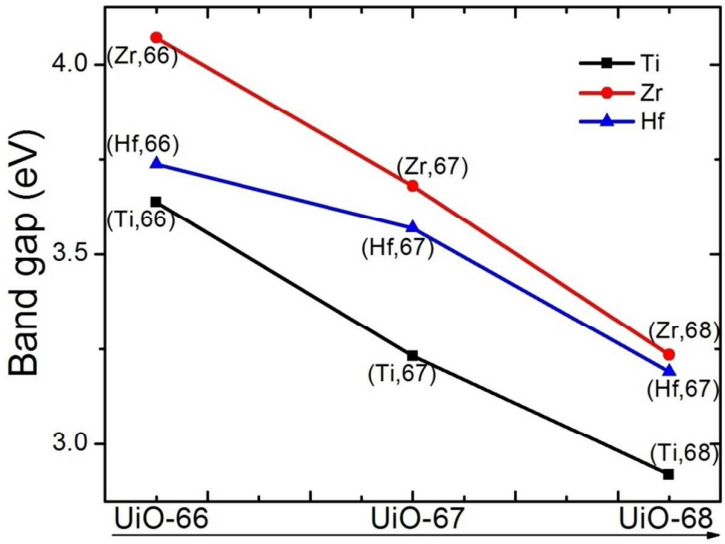


Metal-organic frameworks UiO-66, 67, 68 and analogues have exceptional thermal and chemical stability, are resistant to water, acid, and base for use in real-world applications.